Growth mechanism of highly twinned Al13Fe4 dendrites obtained from a rapidly solidified Al-5at.% Fe melt

D Dubaux, Julien Zollinger, M-C de Weerd, J Ghanbaja, S Mathieu, S Migot, P Boulet, S Šturm, V Fournée, M Sicot, et al.

Growth mechanism of highly twinned $Al_{13}Fe_4$ dendrites obtained from a rapidly solidified Al-5at.% Fe melt

D. Dubaux[a,c], J. Zollinger[a,c], M.-C. de Weerd[a,c], J. Ghanbaja[a,c], S. Mathieu[†a,c], S. Migot[a,c], P. Boulet[a,c], S. Šturm[b,c], V. Fournée[a,c], M. Sicot[a,c], J. Ledieu[a,c]

[a] *Université de Lorraine, CNRS, IJL, F-54000 Nancy, France*
[b] *Jožef Stefan Institute, Department for Nanostructured Materials, Jamova Cesta 39, 1000 Ljubljana, Slovenia*
[c] *International Associated Laboratory PACS2, CNRS Université de Lorraine, Nancy, France and Jožef Stefan Institute, Ljubljana, Slovenia*

Abstract

We report the formation of large and highly twinned dendrites of the $Al_{13}Fe_4$ approximant phase embedded in an *fcc* Al-rich matrix. Using a rapid cooling technique, the approximant appears as a 10-fold dendrite. Within each arm, all grains share a common [010] direction. The grain distributions within the arm are quite complex and a single dendrite arm can contain up to four different orientations. Using several techniques, including Electron Back-Scattered Diffraction (EBSD) and Transmission Electron Microscopy (TEM), it has been possible to identify three types of twins, namely $\{100\}$, $\{001\}$ and $\{20\bar{1}\}$ twins. From these observations and previous reports, we propose a growth mechanism to explain the formation of such specific 10-fold motifs. It corresponds to the heteroepitaxial growth of the $Al_{13}Fe_4$ approximant from a well-facetted decagonal Al-Fe quasicrystalline seed.

Keywords: A. intermetallics; B. nucleation and growth, twinning; C. rapid-solidification; D. grain boundaries; E. electron backscatter diffraction

1. Introduction

The proportion of scrap used for aluminium production will continually increase in the coming decades [1]. With recycling, the amount of iron continually increases in aluminium alloys [2], and it is important to know its effects on microstructures and properties. Iron is an essential alloying element in a variety of aluminium alloys used for packaging, architecture and lithography [3, 4]. New aluminium alloys with improved temperature capability have been widely investigated for potential use for a variety of aerospace applications [5, 6]. Depending on the cooling rates and the initial alloy stoichiometry, different Al-Fe binary compounds may coexist including metastable and stable phases of various morphologies. For instance, post-heat treatments of Al-2.5 wt% Fe binary alloys produced

[†] Deceased

by laser powder bed fusion (L-PBF) technique contain particles of the metastable Al_6Fe phase and needle- or plate-shaped stable $Al_{13}Fe_4$ phase. This L-PBF technique in which laser selectively irradiates on successive Al-Fe alloy bedded layers enables very high cooling rates during solidification and represents an alternative process to synthesize Al alloys of improved mechanical properties [7]. Other approaches used to obtain metastable and stable Al-Fe phases embedded in an Al-rich matrix include for instance arc melting and melt spinning techniques.

The growth of Al-Fe binary phases can also occur fortuitously at coating interfaces. When hot-dip aluminizing of steel and cast-iron, the coating microstructure consists of an outer layer of molten bath composition and an inner intermetallic layer containing aluminium and iron elements. This inner layer present two zones with $Al_{13}Fe_4$ and Al_5Fe_2 phases respectively adjacent to the outer layer and to the cast-iron or steel substrate [8]. The influence of reaction temperature and time on the thickness and growth kinetics of the $Al_{13}Fe_4$ has been recently investigated [9]. Indeed, it is of importance to understand the Al-Fe phase formation and interfacial microstructure evolution in several industrial process including hot-dip aluminizing, die casting or weld brazing to name of few.

The $Al_{13}Fe_4$ compound is often identified as the brittle intermetallic in Al alloys affecting the formability and resistance of the end product [10]. Using X-ray diffraction measurements, Black [11] determined the $Al_{13}Fe_4$ crystal structure and highlighted the complexity of the system with the presence of (100) and (001) glide twin models. This followed the first report by Groth [12] of (100) and (001) reflection twins observed by optical microscopy. As reported by Mondolfo [13], the monoclinic structure of $Al_{13}Fe_4$ was initially observed as containing 100 atoms per unit cell until more recently [14]. Adam *et al.*[15] reported the evolution of the crystallographic relationships between the Al-$Al_{13}Fe_4$ eutectic phases, the $Al_{13}Fe_4$ microstructure and the associated twinning mechanism for various imposed temperature gradient (G) to growth rate (R) ratio. In their study, it was demonstrated that for low G/R the $Al_{13}Fe_4$ plates branched frequently while this was suppressed with increasing G/R ratio. In addition, twin plane re-entrant edge mechanism was proposed for the growth of $Al_{13}Fe_4$ plates. Later, for rapidly solidified Al-14at.%Fe alloy, Fung *et al.* [16] reported the coexistence of tenfold $Al_{13}Fe_4$ twins and decagonal quasicrystal. The ten $Al_{13}Fe_4$ dendrites were shown to share a common [010] direction. Their study confirmed the existence of $(20\bar{1})$ twinning as another possibility along (100) and (001) twins as initially proposed by Louis *et al.* [17] to explain the star-shaped $Al_{13}Fe_4$ microstructure. Since, several models [18, 19] have been proposed to explain the ten-arm morphology of the intermetallic, including a model based on (100)-$(20\bar{1})$ fivefold twins [19]. All atomic models of the twins identified in $Al_{13}Fe_4$ and more generally in $Al_{13}M_4$ (M=Fe, Pd, Co) are described by Saito *et al.* [20]. Twinning and planar lattice defects were also observed for $Al_{13}Fe_4$ compounds solidified from the gas phase obtained by evaporating an Al-Fe alloy in Xe gas [21].

All these studies demonstrate the complexity and numerous morphologies associated with the growth of the $Al_{13}Fe_4$ phase in Al-rich matrix depending on the synthesis conditions. From a hypereutectic Al-Fe alloy rapidly solidified, we report the growth of highly twinned 10-fold dendrites of $Al_{13}Fe_4$ phase. A systematic study of the crystallographic orientations of the $Al_{13}Fe_4$ phase was carried out to gain information on the preferred arm growth direction, on the twinning relationships among adjacent grains and on the origin of the dendrite nucleation.

After a description of the experimental details in Section 2, the main results obtained from a multi-technique approach will be presented in Section 3. Before the conclusion, the results will be discussed in Section 4 and a growth mechanism for the 10-fold dendrites will be proposed.

2. Experimental details

The Al-Fe samples have been synthesized by arc-melting under a partial argon atmosphere (700 mbar) from high purity Fe and Al metals (>99.8%). The elements in the form of platelets are placed on a water-cooled copper hearth (anode) to limit heat exchange. To minimise material loss, aluminium having the highest vapour pressure is covered by iron shots. Note the large material density difference (Al: 2.7 g.cm^{-3} and Fe: 7.8 g.cm^{-3}) and melting temperature (Al: 933 K and Fe: 1808 K). The sample obtained is turned over and remelted several times to ensure its homogeneity, which could be compromised *a priori* by the strong thermal gradient between the point of impact of the arc and the crucible. An activated (pre-heated) Zr-Ti button acting as an oxygen getter was placed on the copper hearth away from the Al-Fe preparation. The arc-melter was stopped abruptly to favor a high cooling rate and potentially trap metastable phases. Initially, an Al-Fe primary sample was prepared with the compositions Al-95 at.% (Al-90.2 wt. %). The Al-rich atomic composition is selected to explore which (meta)-stable phases will be present under the present preparation conditions. For instance, can the metastable Al_6Fe or Al_9Fe_2 [22, 23] phase be synthesized for these compositions?

Following the synthesis, the sample has been studied using standard metallographic techniques, optical microscopy and scanning and transmission electron microscopy techniques (SEM/TEM). For microscopic observations, a millimeter-thick slice has been cut from the $Al_{95}Fe_5$ ingot. The final polishing step was performed with a colloidal silica suspension (0.05μm) to obtain a mirror-like surface. The local composition of the phases have been determined by energy dispersive X-ray spectroscopy (EDS). The SEM is also equipped with an electron back-scattered diffraction (EBSD) detector for a quantitative characterization of the microstructures of the mirror-polished polycrystals and to determine the grain orientation within the materials. The EBSD measurements have been performed using a ZEISS GeminiSEM 500 equipped with a Symmetry CMOS EBSD detector from Oxfords Instruments. The Aztec software (Oxford Instruments) has been used for data acquisition and phase indexing. A step size of 170 nm has been chosen for the measurements. The data analysis has been carried out using the HKL Channel 5 program suite by Oxford Instruments. For the TEM analysis, electron transparent lamellae have been prepared by focus ion beam (FIB). The characterisation of the phases was carried out using powder X-ray diffraction (PXRD) on a D8 Advance Bruker diffractometer using Cu K_{α_1} radiation (λ = 1.54056 Å). Some powder was extracted from the ingot by scraping its surface with a diamond saw and an X-ray diffraction pattern was recorded in the 10° to 100° 2θ range. The EVA software (Bruker Company) was used to simulate the "Intensity" diagrams (in arbitrary units) as a function of the angle 2θ.

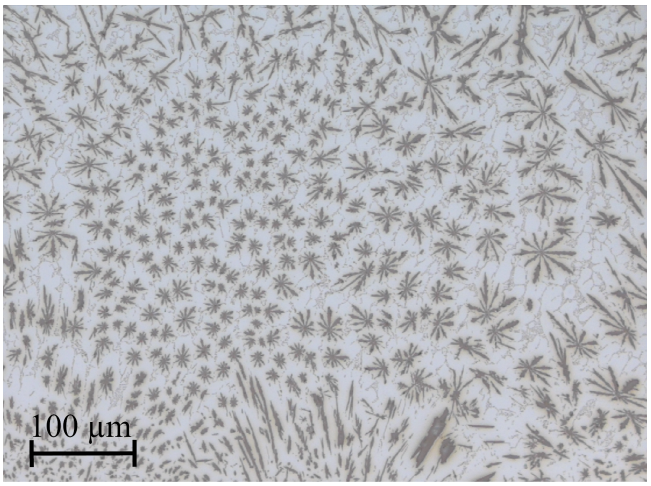

Figure 1: Optical micrograph of a slice through the $Al_{95}Fe_5$ button with the different 10-fold dendritic and acicular morphologies observed.

3. Results

3.1. Optical and scanning electron microscopy observations

The optical microscopy observations on $Al_{95}Fe_5$ reveal the presence of numerous almost complete 10-fold branched dendritic particles (hereafter referred as 10-fold dendrites) surrounded by eutectic cells of Al (see Figure 1). A higher density of such 10-fold dendrites is found on the button side in contact with the water-cooled copper hearth (i.e. higher cooling rate).

The later cells are also located in the interdendritic regions. The 10-fold dendrite branching begins some distance from the particle core before propagating into the Al-rich matrix[17]. These features are reminiscent to the tenfold twins reported by Fung *et al.* [16] while studying rapidly cooled Al-Fe alloys obtained by melt-spinning method. In other parts of the sample, the facetted 10-fold dendrites are less developed and the morphology is dominated by elongated needle-like features. As seen in Figure 2, the latter are particularly well identified using SEM techniques. The chemical analyses performed by EDX on the needles and 10-fold dendrite arms lead to an atomic composition of 70 to 75 at.% aluminium and 30 to 25 at.% iron. From the Al-Fe phase diagram and the EDX uncertainty, these stoichiometries would be consistent with the stable Al_5Fe_2 and/or $Al_{13}Fe_4$ phases but not with any reported Al-Fe metastable phases. The oxygen concentration is relatively low and seems to be slightly higher in the needle and petal vicinity.

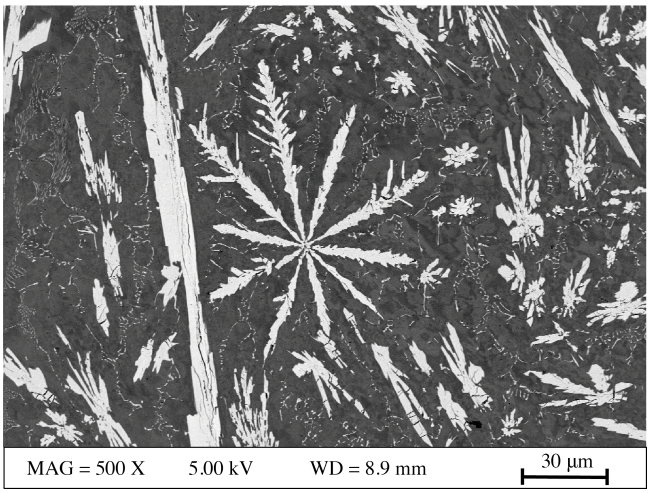

Figure 2: SEM image showing a region where large and small 10-fold dendrites can be distinguished.

3.2. *Powder X-ray diffraction analysis*

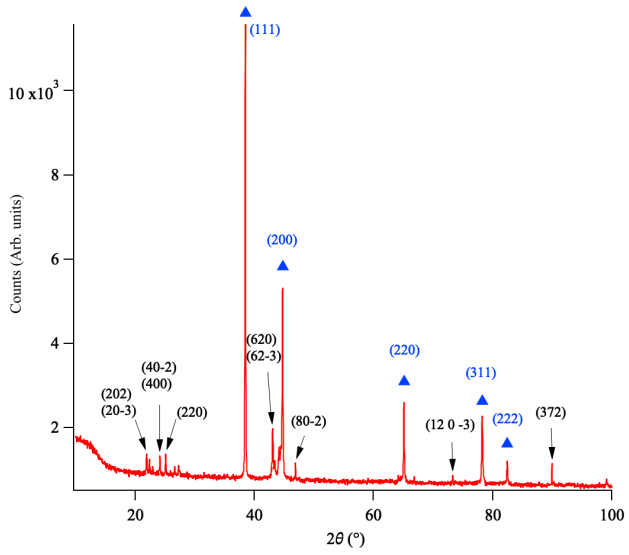

Figure 3: Powder X-ray pattern recorded for the $Al_{95}Fe_5$ sample revealing the presence of Al-*fcc* ($Fm\bar{3}m$) and $Al_{13}Fe_4$ ($C2/m$) phases. The peaks marked by blue triangles are assigned to the Al-*fcc* while the other peaks are associated to the approximant phase. For clarity, only the most intense peaks of the $Al_{13}Fe_4$ phases have been indexed on the diffractogram.

The $Al_{13}Fe_4$ compound is a well-known approximant to the decagonal quasicrystal which exhibits a four-layer periodicity along the pseudo-ten-fold axis. It crystallizes in the $C2/m$ monoclinic space group. The unit cell contains 102 atoms and has the following lattice parameters: a = 15.492 Å, b = 8.078 Å, c = 12.471 Å with β = 107.69° [14]. Apart from these two systems, no other phases could be detected in the powder X-ray diffraction pattern. Note that

the presence of two phases such as Al_6Fe (metastable) and Al_5Fe_2 (stable) compounds have been identified in sample with respectively 2 at.% and 10 at.% Fe that we have prepared under the same arc-melting conditions.

3.3. Characterisation by TEM

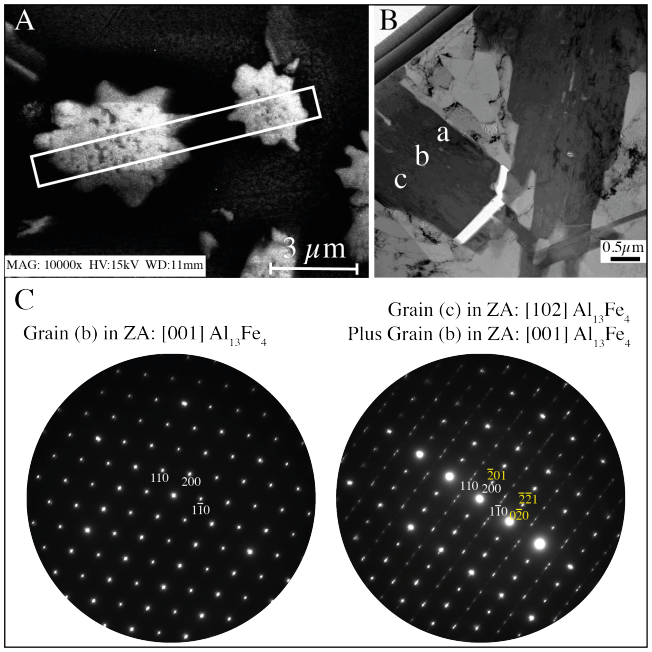

Figure 4: (A) SEM image showing the area where the FIB lamella was taken (white rectangle). (B) Cross-sectional view of the FIB lamella. (C) SAED patterns Grain *b* - zone axis (ZA) [001](C-left); Grain *b* - ZA [001] and Grain *c* - ZA [102] (C-right).

In order to complete the SEM and PXRD measurements, a FIB lamella bisecting the cores of two 10-fold dendrites has been cut and investigated by Scanning TEM (STEM) and selected area electron diffraction (SAED) techniques. As shown in Figure 4(A), small 10-fold dendrites, with underdeveloped arms, have been selected as they should represent the initial stages of the approximant growth/nucleation. Thus, their core may contain additional (meta)-stable phases undetected by PXRD. As demonstrated by cross-sectional observations of the FIB lamella by TEM (see Figure 4(B)), the two small 10-fold dendrites appear to intersect beneath the surface. The elongated grains labelled *a*, *b*, *c* in Figure 4(B) are adjacent to each other and arrange in parallel to form part of the 10-fold dendrites. Qualitatively, EDXS mapping carried out on the three grains reveals that those are composed of aluminium and iron while the matrix consists in almost pure aluminium. The quantitative analysis gives an atomic percentages of 75% of Al and 25% of Fe, which is consistent with the exclusive presence of the $Al_{13}Fe_4$ phase within the 10-fold dendrites.

The different grain orientations have been determined using SAED technique. As shown in Figure 4(C), the pattern of the central grain *b* has been acquired in the $[001]_{Al_{13}Fe_4}$ zone-axis. The orientations of grain *a* and *c* are

identical and viewed along the $[102]_{Al_{13}Fe_4}$ zone-axis (only shown here for grain *c*). These results demonstrate a specific structural relationship between [001] and [102] $Al_{13}Fe_4$ directions. If grains *a* and *c* correspond indeed to diametrically opposite arms of the 10-fold dendrites, then they share a common orientation. These orientations are also consistent with the domain twinning relationship presented in Fig.7(b) where for instance [001] (orange domain) and [102] (green domain) directions will be colinear to each other. In addition, these SAED patterns demonstrate that both $[001]_{Al_{13}Fe_4}$ and $[102]_{Al_{13}Fe_4}$ directions are perpendicular to the 10-fold axis of the dendrites as confirmed in Fig.5(b) and Fig.6(b,c).

3.4. EBSD analysis

To further analyse these intrinsic structural relationships, EBSD measurements were carried out on a large ten-fold dendrite as shown in Figure 5(A). The entire dendrite could be indexed to the $Al_{13}Fe_4$ phase in agreement with XRD and TEM measurements. Figure 5 shows different orientations within each arm. Another striking feature is the similar orientations shared by opposite arms, as evidenced by the associated grain colours. These observations are consistent with recent work by Cui *et al.* [24]. In their studies, the domain orientations are also repeated on the opposite side of the 10-fold grain they characterised. Figure 5(B) shows the corresponding pole figures (PF) of the main crystallographic directions, *i.e.* $\langle 100 \rangle$, $\langle 001 \rangle$ and $\langle 010 \rangle$. Following the $\langle 100 \rangle$ and $\langle 001 \rangle$ directions, each grain is rotated with its neighbour by 36°, which is compatible with decagonal symmetry. All indexed grains have a common $\langle 010 \rangle$ direction, as previously reported by several authors [16, 24, 25] (coincidence at a single central point). In the last PF, the black arrows correspond to the ten dendrite growth directions observed in the microstructure, the directions of the $\langle 100 \rangle$ and $\langle 001 \rangle$ poles are indicated by red circles, while the common $\langle 010 \rangle$ pole is indicated by a black circle. This shows that the visible growth directions do not seem to correlate with the low-index directions, which are usually the growth directions [26].

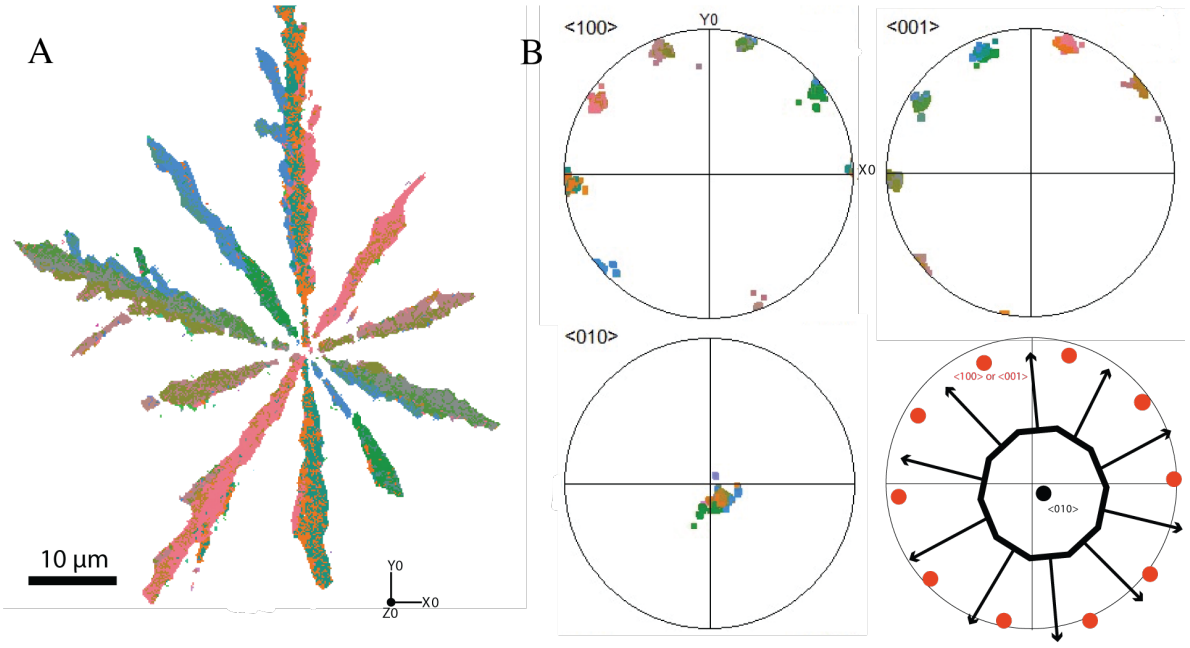

Figure 5: (A) EBSD false colours map (Euler orientation map) of the 10 arms dendrite. (B) Corresponding $\langle 100 \rangle$, $\langle 001 \rangle$ and $\langle 010 \rangle$ pole figures. The last pole figure summarizes the position of the $\langle 100 \rangle$, $\langle 001 \rangle$ (red circles) and $\langle 010 \rangle$ (black circle) while the black arrows indicate the actual dendrite arms growth directions (see text for details).

A closer examination of one dendritic arm was performed to further investigate the growth crystal directions and mechanism, corresponding to the large upper arm in Figure 5(A), which contains 4 different grain orientations. As shown in Figure 6(A), two grains (dark green and orange respectively) appear alternately along the central part of the arm. Two other grain orientations (blue and pink) have been identified to the left and right of the central region. Figure 6(B) shows a PF with the corresponding $\langle 001 \rangle$ and $\langle 010 \rangle$, with the apparent direction of growth indicated by a black arrow. The corresponding $\langle 001 \rangle$ directions have been included in Figure 6(A). This direction appears to be the growth direction, especially for the blue and pink grains in the image. Why does the $\langle 001 \rangle$ direction not correspond to the actual growth direction? Figure 6(C) shows the $\langle 100 \rangle$, $\langle 102 \rangle$ PF corresponding to the four grains. The dark green and orange grains share a common $\langle 100 \rangle$, while the blue and pink grains are rotated by +36° and -36° respectively. The $\langle 102 \rangle$ PF shows that the $\langle 102 \rangle$ direction of the orange grain corresponds to the $\langle 001 \rangle$ direction of the dark green grain, and vice versa.

The difference between the overall dendrite arm direction and the $\langle 001 \rangle$ crystal growth direction can be understood by considering that the $Al_{13}Fe_4$ phase has nucleated from a decagonal quasicrystal (*d*-QC) with the following orientation relationships: (i) $\langle 010 \rangle_{Al_{13}Fe_4} \parallel [001\bar{1}0]_{d\text{-QC}}$ 2-fold symmetry axes; (ii) $\langle 001 \rangle_{Al_{13}Fe_4} \parallel [00001]_{d\text{-QC}}$ 10-fold symmetry *d*-QC axis and (iii) $\langle 100 \rangle_{Al_{13}Fe_4} \perp [10000]_{d\text{-QC}}$ 2-fold symmetry axes. While the latter will be discussed in detail in section 4, it is illustrated in Figure 6(D). Assuming nucleation on a *d*-QC, the dendrite analysed in Figure 6 is likely to have nucleated on the upper facet of the partial decagon shown in Figure 6(D). From the orientation

relationships above, the dark green and orange grains have the same probability of nucleation from the *d*-QC. The blue and pink grains have the same crystal growth directions as the dark green and orange grains respectively, but it is still unclear why they appear. The answer lies in the fact that one of the growth mechanisms of $Al_{13}Fe_4$ is twinning [24]. While it is poor at low growth rates, it can become more dominant at high growth rates for faceted crystals [27]. From the results presented in Figure 6(B-D) several clues can be observed to determine the relationship between the twinning orientations:

- the dark green and orange grains have a common $[100]$ orientation,
- the blue and dark green grains, and the orange and pink grains respectively, share a common $[001]$ direction,
- the $[102]$ directions of the orange and dark green grains are parallel to the $[001]$ directions of the dark green/blue and orange/pink grains, respectively.

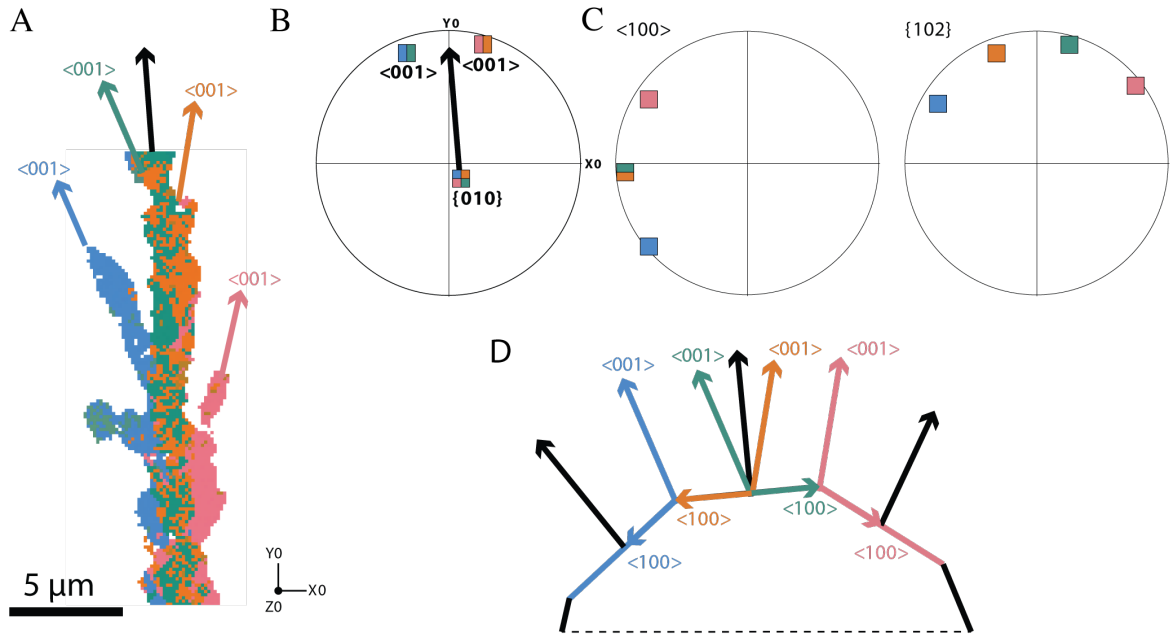

Figure 6: (A) EBSD false colours map for one of the arms of the 10-fold dendrite having 4 different grains, (B) Reconstructed pole figures showing the $\langle 001 \rangle$ directions (indicated by colored arrows in (A)) and the $\{010\}$ planes corresponding to an average orientation for each grain orientation. The apparent growth direction of the whole dendrite branch is indicated with a black arrow, (C) corresponding $\langle 100 \rangle$ and $\langle 102 \rangle$ pole figures, (D) schematic representation of the crystal direction on a partial view of a decagon.

The [001] directions of the dark green and orange grains are actually at 144° ($180° - 36°$). The [102] directions of the orange and dark green grains are parallel to the [001] directions of the dark green/blue and orange/pink grains respectively (see Figure 7(A)). These analyses lead to the determination of the respective orientations and the twinning

relationship that exists between the largest grains in the arm. For example, Figure 7(B) shows the existence of (100) twinning planes between pink/orange and also dark green/blue grains. Furthermore, a double twinning along first $(20\bar{1})$ and then (001) planes transforms the orange to the blue grain. It is important to note that the $(20\bar{1})$ plane is parallel to the [102] direction. The same operation ($(20\bar{1})$ followed by (001) planes) is valid to change the dark green to pink grain. During growth, a succession of parallel twins (i.e. within the same plane) may occur, as observed in the central region of the arm (change from dark green to orange grains). The configuration is different when the second twin is in a different plane. The growth of this reoriented grain is likely to join other boundaries, creating a secondary twin. This is probably the scenario in the present case and could explain the twinning relationships observed between the orange/blue grains and also the dark green/pink grains. Although not shown here, the same analysis performed on this arm can be applied to the other nine dendrite arms. These EBSD results are of paramount importance for understanding the nucleation and growth mechanisms of the 10-fold $Al_{13}Fe_4$ dendrites. The grains with a common habit plane grow in a zigzag manner by twinning with a 180° rotation of the $\langle 100 \rangle$ directions along the $[010]$; the grains with a common $\langle 001 \rangle$ growth direction have a 180° rotation around this direction ((100) twinning). Grains with no common plane or direction are accommodated by twinning around the $(20\bar{1})$ and then (001) planes.

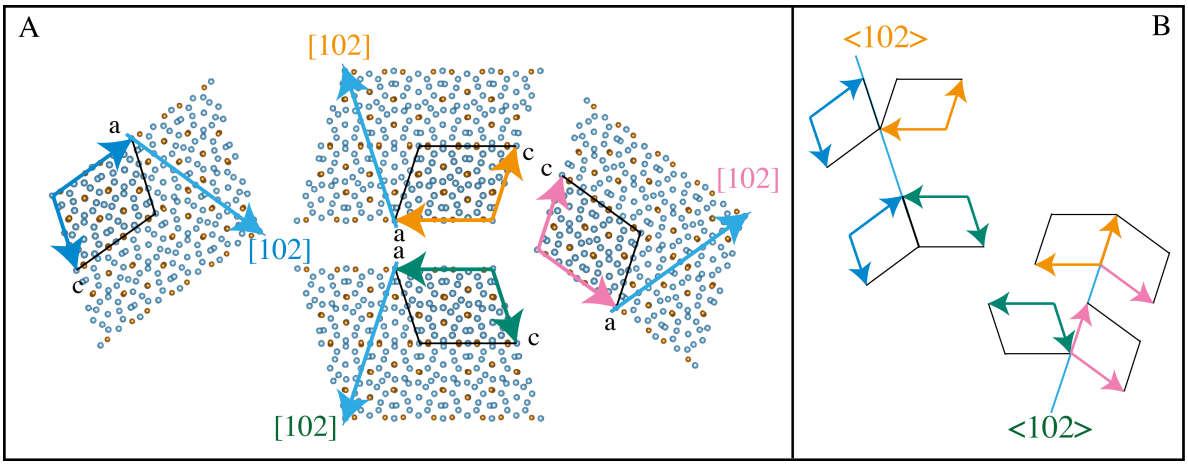

Figure 7: (A) Orientations of the four different grains exposing their $Al_{13}Fe_4$(010) planes. (B) Twinning relationship among the four domains within the same arm. The blue, orange, pink and dark green lattice vectors are gathered by pairs to visualise the twinning relationship identified.

4. Discussion

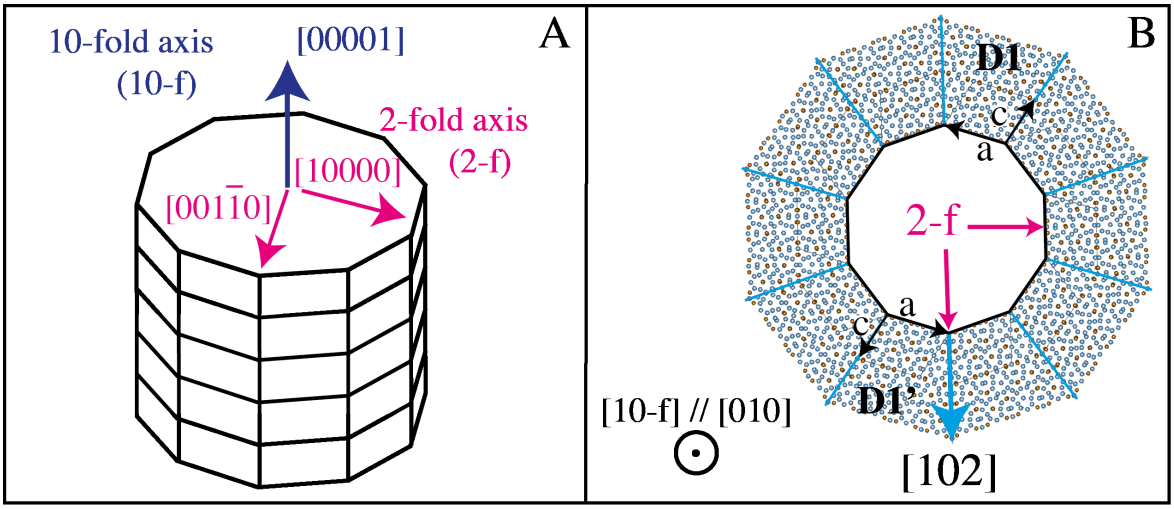

Figure 8: (A) Schematic representation of a decagonal quasicrystal where quasiperiodic layers are stacked periodically along the [00001] direction (10-f axis). (B) Model illustrating the hypothetical growth of the $Al_{13}Fe_4$ 10-fold dendrite, starting from a decagonal seed. The 10-f axis of the *d*-quasicrystal and the [010] (referred as pseudo-10-fold (p-10-f)) direction are parallel. Around the central germ constituted by the decagonal phase, grow the ten arms of the dendrites. Their *c* axes are distributed every 36°.

By rapid solidification of Al-Fe binary mixtures with a very high content in Al (85 to 95 % at.), a whole variety of complex phases ranging from metastable (for example decagonal, tetragonal centered Al_mFe, monoclinic Al_9Fe_2, orthorhombic Al_6Fe) to stable phases ($Al_{13}Fe_4$,...) can be potentially synthesized. This variety is related to different factors including the initial mixture composition and the cooling rate [28–31]. Hence, several metastable and stable phases may coexist within the same sample depending on the growth/synthesis technique used. This is precisely what Fung *et al.* [16] observed by TEM observations on an Al-14at.%Fe alloy obtained by rapid solidification. This study reported the formation of $Al_{13}Fe_4$ tenfold twins (10-fold dendrite) with all arms sharing a common [010] direction. The arms exhibited by TEM numerous stacking faults contrast bands perpendicular to the growth direction. More importantly, high resolution images demonstrated the coexistence of the decagonal Al-Fe and the $Al_{13}Fe_4$ approximant phases with the $[010]_{Al_{13}Fe_4}$ direction being parallel to the 10-fold axis of the decagonal quasicrystal. At this stage, it is important to recall the structural relationship between the two complex phases. With 102 atoms per unit cell, the $Al_{13}Fe_4$ structure can be described along the [010] direction as a stacking of flat planes (F) and puckered planes (P) in the sequence $F_{0.0}P_{0.25}F_{0.5}P_{0.75}$ (the subscript standing for the y coordinate). The periodicity along the *b* axis is 8.078 Å and each plane presenting a pseudo-10-fold (p-10-f) symmetry. In 3-dimensions, the structure can be described geometrically by 23-atom pentagonal bipyramid clusters [32]. Concerning the aperiodic system, the *d*-Al-Fe structure can be described as a periodic stacking (period equal to $2\times b$ = 1.65 nm [16]) along the direction [00001] of 10-fold quasiperiodic planes. The as-grown decagonal single grains usually exhibit ten well-defined facets

as shown and depicted in Figure 8(A) as is the case for *d*-Al-Ni-Co grain described by Fisher [33]. Two non-equivalent two-fold (2-f) directions (Figure 8(A)), namely [001$\bar{1}$0] and [10000] lie perpendicular to the 10-fold axis. From these structural descriptions, the orientation relationship $[010]_{Al_{13}Fe_4} \parallel [00001]_{d\text{-}QC}$ appears highly coherent considering the match between both periods. Hence, it is not surprising that annealing of the Al-14-at.%Fe alloy *in situ* resulted in the thermal decomposition of *d*-Al-Fe into the $Al_{13}Fe_4$ approximant phase [16].

Later, similar ten-fold twinned $Al_{13}Fe_4$ have also been identified by Kim *et al.* [28] on melt-spun ribbons of initial composition Al-15-at.%Fe post-annealed to 753 K for 15 min. As explained above, this study illustrates the possibility to obtain metastable phases for different compositions ranging from 5 to 15 at.% Fe and for various cooling rates. Thus, the metastable microquasicrystalline, decagonal, Al_mFe, as well as Al_6Fe phases appeared in order of increasing thermodynamic stability. The microquasicrystalline phase (sample Al-5at.%Fe) consists of clusters of nanometer-scale randomly oriented icosahedral particles [28].

In the present work, the 10-fold dendrite in Figure 5 have been obtained by arc melting for an initial composition of Al-5at.%Fe, i.e. with a lower cooling rate and Fe content than previously reported [16, 28]. Compared to the works cited above, important differences can be highlighted on the larger length scale of the dendrites than reported by melt spinning, the twin types present among the grains and the absence of metastable phase, with only stable phases Al and $Al_{13}Fe_4$ phases being detected. In line with the work of Hiraga *et al.* [20], we mainly find twin planes (100) and (001) but also indirectly (20$\bar{1}$). It should be recalled here that twins are intrinsic to the $Al_{13}Fe_4$ system and are also found in single crystals obtained by Czochralski growth. The EBSD maps demonstrate the presence of dendrites with a [001] growth axis. This preferential growth orientation is particularly visible for the elongated blue and pink grains (see Figure 6(A)). The alternance between dark green and orange grains at the arm center (Figure 6(A)) translates into a zig-zag of the *c* axis along the dendrite.

From the observations of Fung *et al.* [16], the decagonal Al-Fe and the growth of the 10-fold dendrite of the approximant $Al_{13}Fe_4$ are intrinsically linked but how can we explain this particular growth? During the synthesis of our sample, we can initially expect the presence of an icosahedral local order (ISRO for Icosahedral Short Range Order) in the liquid phase. Proposed by Frank [34] to explain the significant supercooling observed in many metals, this ISRO has been highlighted in several metals in melting and supercooling states but also for a composition leading to the formation of the decagonal quasicrystal $Al_{65}Cu_{25}Co_{10}$ [35]. Moreover, additional works on interfacial energies on *d*-$Al_{65}Cu_{25}Co_{10}$ and icosahedral (*i*)-$Al_{60}Cu_{34}Fe_6$ quasicrystals have highlighted a much lower interfacial energies for the quasicrystalline phases than for normal crystalline phases. The reason given is a greater structural similarity between the melt and quasicrystalline solid [36]. It is likely that a similar mechanism is present in the Al-Fe system for which nanometer-scale randomly oriented icosahedral particles have already been identified [28].

It is therefore reasonable to postulate that the aperiodic phase will grow from local icosahedral order leading to decagonal grains of high structural quality as observed by Fung *et al.* [16]. Decagonal quasicrystals are usually highly faceted with easily distinguishable 2-fold facets (see also Figure 4 in reference [33] and Figure 1(B) in reference [37] for micrometer-size faceted decagonal quasicrystals). The decomposition of the decagonal phase into the approximant phase has been confirmed and observed *in situ* by Fung *et al.* [16]. Thus, we propose that during this decomposition, the growth of the $Al_{13}Fe_4$ phase starts on the 10 facets of a nanometer-size decagonal grain. The natural orientation between the quasicrystal and the approximant phases leads to parallel 10-f and p-10-f axes. From a careful inspection of Figure 6, the $\vec{c}$ and -$\vec{c}$ directions appear as rapid growth directions. Hence, the $Al_{13}Fe_4$ compound tends to grow from the ($\vec{a}$,$\vec{b}$) plane which would minimize its interfacial energy. As the $\vec{c}$ axis is not being perpendicular to this plane, repetitive twins will occur to maintain a rapid growth and to maximize the ($\vec{a}$,$\vec{b}$)-to-liquid interface, as seen in Figure 7. The $Al_{13}Fe_4$(010) planes are then parallel to the two-dimensional quasicrystalline planes (see Figure 8(B)). Under our synthesis conditions, the disappearance of the decagonal phase is total. In this nucleation scenario, the orientation of opposite grains (see D1 and D1' in Figure 8(B)) would be identical, hypothesis confirmed experimentally by EBSD measurements. The [102] direction of a domain is here parallel to the direction [001] of the adjacent domain in the counter-clockwise direction. These specific directions are themselves aligned with the 2-f [001$\bar{1}$0] axis.

5. Conclusion

In conclusion, rapid cooling of an Al-Fe mixture (Al-5%at.Fe) obtained by arc-melting can lead to the growth of the $Al_{13}Fe_4$ approximant in the form of 10-fold arms embedded into an Al-rich matrix. No quasiperiodic phase could be detected in the sample. Using EBSD measurements, it has been possible to determine the twinning relationships between the grains present within the dendrites with $\{100\}$, $\{001\}$ and $\{20\bar{1}\}$ twins being identified. All grains analysed share a common [010] direction and appear to grow in the [001] direction. A high density of (001) twins perpendicular to the arm rapid growth direction are distinguishable. Regarding the 10-fold dendrite growth mechanism, ISRO in the liquid could possibly precede the nucleation of a well-facetted decagonal Al-Fe grain. Then, the latter will decompose into the $Al_{13}Fe_4$ approximant which will grow from the *d*-Al-Fe facets. From their structural similarity, the *d*-Al-Fe / $Al_{13}Fe_4$ natural orientation will lead to 10-f $\parallel$ p-10-f axes. The approximant phase will grow from (a,b) planes to minimise the interfacial energy. As the [001] direction is not perpendicular to this plane, twins occurs to maximise the (a,b) interface. These successive nucleation steps are necessary to understand the microstructure composed of 10 arms. They are reminiscent to the hypothesis formulated by Kurtuldu and Rappaz [38–40] to explain the large number of neighboring grains in a twin relationship in the Cr:Al-Zn and Ir:Au-Cu-Ag systems. The addition of a minute amount of Cr and Ir leads to a refinement of the *fcc* grains. The latter present orientation relationships compatible with the icosahedron or with interlocked icosahedron geometry [38]. For the Al-Zn system, the authors concluded to a heteroepitaxial growth of the *fcc* grains from the faces of an icosahedral quasicrystalline

phase with the following relationship: $111_{fcc} \mid 110_{fcc} \perp$ 3-fold $\mid$ 2-fold. This work is coherent with the existence of icosahedral quasicrystalline phases preceding the formation of *fcc* grains, but also its importance on nucleation and the twin relationships obtained between neighboring grains. In comparison to the works reported by Kurtuldu *et al.* [38], the origin of the 10-fold dendrite should be considered as the result of a heteroepitaxial growth of a decagonal approximant on a decagonal Al-Fe quasicrystalline template. Similar to previous works [35], it is foreseen that elastic neutron scattering experiment carried out for various $Al_{95}Fe_5$ melt temperatures could bring further evidences of the existence of ISRO in the liquid state.

Acknowledgments

This work is supported by the European Integrated Center for the development of New Metallic Alloys and Compounds.

References

[1] D. Raabe, C.C. Tasan, E.A. Olivetti, Strategies for Improving the Sustainability of Structural Metals, Nature 575 (2019) 64–74.

[2] Mark E. Schlesinger, Aluminum Recycling, CRC press, 2013.

[3] C. Allen, S. Kumar, L. Carrol, K. O Reilly, H. Cama, Electron Beam Surface Melting of Model 1200 Al Alloys, Mater. Sci. and Eng. A 304-306 (2001) 604–607.

[4] N. Belov, A. Aksenov, D. Eskin, Iron in Aluminium Alloys: Impurity and Alloying Element, Taylor, Francis (Eds), Publishing London, 2002.

[5] W. Boettinger, L. Bendersky, F. Early, An Analysis of the Microstructure of Rapidly Solidified Al-8 wt pct Fe Powder, Metall. Trans A 17 (1986) 781.

[6] H. Jones, The Status of Rapid Solidification of Alloys in Research and Application, J. Mater. Sci. 19 (1984) 1043–1076.

[7] X. Qi, N. Takata, A. Suzuki, M. Kobashi, M. Kato, Change in Microstructural Characteristics of Laser Powder Bed Fused Al-Fe Binary Alloy at Elevated Temperature, J. Mat. Sci. and Technol. 97 (2022) 38–53.

[8] R. Mola, T. Bucki, K. Wcisło, Characterization of Coatings on Grey Cast Iron Fabricated by Hot-dipping in Pure Al, AlSi11 and AlTi5 Alloys, Arch. Foundry Eng. 14 (2014) 85–90.

[9] H. He, L. Zhang, Z. Liu, W. Zhao, Kinetics of Intermetallic Compound Layers between AISI 321 Stainless Steel and Molten Aluminum, Mater. Charact. 203 (2023) 113062.

[10] C. Allen, K. O'Reilly, B. Cantor, P. Evans, Intermetallic Phase Selection in 1XXX Al Alloys, Prog. Mater. Sci. A 43 (1998) 89–170.

[11] P. Black, The Structure of $FeAl_3$, Acta Cryst. 8 (1955) 43.

[12] P. Groth, An Introduction to Chemical Crystallography, Gurney, Jackson (Eds), 1906.

[13] L. Mondolfo, Aluminium Alloys: Structure and Properties, Butterworth, Heinemann (Eds), 1976.

[14] J. Grin, U. Burkhardt, M. Ellner, K. Peters, Crystal Structure of Orthorhombic $CoAl_{13}$, J. Alloys Compd. 206 (1994) 243.

[15] C. Adam, L. Hogan, Cristallography of the Al-Al_3Fe Eutectic, Acta Metallurg. 23 (1975) 345.

[16] K. Fung, X. Zou, C. Yang, Transmission Electron Microscopy Study of $Al_{13}Fe_4$ Tenfold Twins in Rapidly Cooled Al-Fe Alloy, Philos. Mag. Lett. 55-1 (1987) 27–32.

[17] E. Louis, R. Mora, J. Pastor, Nature of Star-shaped Clusters of $FeAl_3$ in Aluminium-Iron Alloys, Metal Sci. 14 (1980) 591.

[18] M. Ellner, U. Burkhardt, Multiple Twinning of $Al_{13}Fe_4$ Showing Pentagonal Pseudosymmetry, Materials Science Forum 150-151 (1994) 97–108.

[19] X. Ma, H. Liebertz, U. Köster, Multiple Twins of Monoclinic $Al_{13}Fe_4$ Showing Pseudo-Orthorhombic and Fivefold Symmetries, Phys. Stat. Sol. A 158-2 (1996) 359–367.

[20] K. Saito, K. Sugiyama, K. Hiraga, $Al_{13}M_4$-Type Structures and Atomic Models of Their Twins, Mat. Sci. Eng. A 294 (2000) 279–282.

[21] M. Tsuchimori, T. Ishimasa, Y. Fukano, Crystal Structures of Small Al-Rich Fe Alloy Particles Formed by a Gas-Evaporation Technique, Philos. Mag. B 66-1 (1992) 89–108.

[22] C. J. Simensen, R. Vellasamy, Determination of Phases Present in Cast Material of an Al-0.5Wt.%Fe-0.2Wt.%Si Alloy, Z. Metallkd. 68 (1977) 428.

[23] D. Dubaux, E. Gaudry, M.-C. de Weerd, S. Šturm, M. Podlogar, J. Ghanbaja, S. Migot, V. Fournée, M. Sicot, J. Ledieu, Metastable Al-Fe Intermetallic Stabilised by Epitaxial Relationship, Appl. Surf. Sci. 533 (2020) 147492.

[24] Y. Cui, C. Gourlay, Growth Twinning and Morphology of $Al_{45}Cr_7$ and $Al_{13}Fe_4$, J. Alloys Compd. 893 (2022).

[25] X. Zou, K. Fung, Orientation Relationship of Decagonal Quasicrystal and Tenfold Twins in Rapidly Cooled Al-Fe Alloy, K. Kuo, Phys. Rev. B 35 (1986) 4526.

[26] J. A. Dantzig, M. Rappaz, Solidification: -Revised & Expanded, EPFL press, 2016.

[27] K. Hyde, A. Norman, P. Prangnell, The Effect of Cooling Rate on the Morphology of Primary Al_3Sc Intermetallic Particles in Al–Sc Alloys, Acta Mater. 49 (2001) 1327–1337.

[28] D. Kim, B. Cantor, Structure and Decomposition Behaviour of Rapidly Solidified Al-Fe Alloys, J. Mater. Sci. 29 (1994) 2884.

[29] R. Young, T. Clyne, An Al-Fe Intermetallic Phase Formed during Controlled Solidification, Scr. Metall. 15 (1981) 1211.

[30] L. Walford, The Structure of the Intermetallic Phase Al_6Fe, Acta Crystallogr. 18 (1965) 287.

[31] E. Hollingsworth, G. Frank, R. Willett, Identification of a New Al-Fe Constituent Al_6Fe, Transactions of the American Institute of Mining, Metallurgical and Petroleum Engineers, Society of Mining Engineers of AIME 224 (1962) 188.

[32] C. Henley, Current Models of Decagonal Atomic Structure, J. Non-Cryst. Solids 153-154 (1993) 172.

[33] I. Fisher, M. Kramer, Z. Islam, T. Wiener, A. Kracher, A. Ross, T. Lograsso, A. Goldman, P. Canfield, Growth of Large Single-Grain Quasicrystals from High-Temperature Metallic Solutions, Mat. Sci. Eng. A 10 (2000) 294.

[34] F. Frank, Supercooling of Liquids, Proc. Roy. Soc. Lond. Ser-Math. Phys. Sci. 215-1120 (1952) 43–46.

[35] D. Holland-Moritz, T. Schenk, V. Simonet, R. Bellisent, P. Convert, T. Hansen, D. Herlach, Short-Range Order in Undercooled Metallic Liquids, Mat. Sci. Eng. 98 (2004) 375–377.

[36] K. Urban, D. Holland-Moritz, D. Herlach, B. Grushko, The Undercooling and Phase Formation Behavior of Melts of Quasicrystal-Forming Alloys, Mat. Sci. Eng. 178 (1994) 293–298.

[37] E. Barber, Chemical Bonding and Physical Properties in Quasicrystals and Their Related Approximant Phases: Known Facts and Current Perspectives, Appli. Sci. 9 (2019) 2132.

[38] G. Kurtuldu, P. Jarry, M. Rappaz, Influence of Cr on the Nucleation of Primary Al and Formation of Twinned Dendrites in Al-Zn-Cr Alloys: Can Icosahedral Solid Cluster Play a Role?, Acta Mater. 61 (2013) 7098.

[39] G. Kurtuldu, A. Sicco, M. Rappaz, Metastable Quasicrystal-Induced Nucleation in a Bulk Glass-Forming Liquid, Acta Mater. 70 (2014) 240.

[40] M. Rappaz, P. Jarry, G. Kurtuldu, J. Zollinger, Solidification of Metallic Alloys: Does the Structure of the Liquid Matter?, Met. and Mat. Trans. A 51 (2020) 2651.